Huang Chen
Department of Mechanical Engineering,
Johns Hopkins University,
223 Latrobe Hall,
3400 North Charles Street,
Baltimore, MD 21218
e-mail: hchen98@jhu.edu

Yuanchao Li
Department of Mechanical Engineering,
Johns Hopkins University,
223 Latrobe Hall,
3400 North Charles Street,
Baltimore, MD 21218
e-mail: yli131@jhu.edu

Subhra Shankha Koley
Department of Mechanical Engineering,
Johns Hopkins University,
223 Latrobe Hall,
3400 North Charles Street,
Baltimore, MD 21218
e-mail: skoley1@jhu.edu

Nick Doeller
Department of Mechanical Engineering,
Johns Hopkins University,
223 Latrobe Hall,
3400 North Charles Street,
Baltimore, MD 21218
e-mail: nwdoeller@gmail.com

Joseph Katz[1]
Department of Mechanical Engineering,
Johns Hopkins University,
122 Latrobe Hall,
3400 North Charles Street,
Baltimore, MD 21218
e-mail: katz@jhu.edu

An Experimental Study of Stall Suppression and Associated Changes to the Flow Structures in the Tip Region of an Axial Low Speed Fan Rotor by Axial Casing Grooves

The effects of axial casing grooves (ACGs) on the performance and flow structures in the tip region of an axial low speed fan rotor are studied experimentally in the JHU refractive index-matched liquid facility. The four-per-passage semicircular grooves are skewed by 45 deg, overlapping partially with the blade leading edge (LE) and extending upstream. They reduce the stall flow rate by 40% compared to the same machine with a smooth endwall. Stereo-particle image velocimetry (SPIV) measurements show that the inflow into the downstream side of the grooves and the outflow from their upstream side vary periodically, peaking when the inlet is aligned with the blade pressure side (PS). This periodic suction has three effects: first, substantial fractions of the leakage flow and the tip leakage vortex (TLV) are entrained into the groove, causing a reduction in TLV strength starting from midchord. Second, the grooves prevent the formation of large-scale backflow vortices (BFVs), which are associated with the TLV, propagate from one blade passage to the next, and play a key role in the onset of rotating stall in the untreated fan. Third, the flow exiting from the grooves causes periodic variations of the relative flow angle around the blade LE, presumably affecting the blade loading. The distributions of turbulent kinetic energy (TKE) provide statistical evidence that in contrast to the untreated casing, very little turbulence originating from the TLV and BFV of one blade propagates across the tip gap to the next passage. [DOI: 10.1115/1.4037910]

Introduction

Casing treatments have been used successfully to delay the onset of stall in axial turbomachines with limited penalty in efficiency [1,2]. Among the different approaches, axial casing grooves (ACGs) have been found to be the most effective [3]. Considerable efforts have already been invested to understand the flow mechanism involved and to optimize the geometry of ACGs. For example, Takata and Tsukuda [4] show experimentally that the stall is delayed only when the ACG is skewed in the direction of the rotor rotation, and that the grooves generate periodic high-speed jets in front of the blade, which increase the incidence angle at the entrance to the passage. Smith and Cumpsty [5] observe that ACG cause a considerable increase in blade loading near the tip, presumably by reorienting the flow. Stereo-particle image velocimetry (SPIV) measurements in a transonic compressor rotor by Brandstetter et al. [6] show that the ACGs generate periodic jets and suppress the tip region blockage. Experimental and numerical studies by Müller et al. [7], using ACGs that are very similar to those used in the present paper, show a 23% increase in stall margin, and associated reduction in tip region blockage. Crook et al. [8] show numerically that the improvement to the stall margin by ACG involves suppression of the tip leakage vortex (TLV)-induced blockage by sucking the low energy fluid and reinjecting it at high speed in front of the passage. Recent studies mostly involve Reynolds-averaged Navier–Stokes simulations. For example, Beheshti et al. [9] show that the ACGs are more effective in rotors with large tip gap. Wilke and Kau [10] associate the improvement with suppression of the tip leakage flow and reduction in TLV strength. Recommendations for groove geometries based on steady-state single passage simulations are provided by Djeghri et al. [11]. They show that the skew angle and axial position of the groove have more impact on the stall margin improvement than the slot depth and shape.

Among the many reasons for the difficulties in understanding why ACGs delay stall, two are particularly evident. First, the processes involved in the onset of stall are not fully understood [12], and are subject for on-going research, e.g., on "modal-type" [13–15] and "spike-type" stall [15–20]. Houghton and Day [21] argue that groove-based casing treatments are most effective in delaying the intermittent spike-type stall. Second, due to challenges in accessing the tip region of turbomachines, there is very limited experimental data on the flow there, with or without grooves. The refractive index-matched facility at JHU addresses this limited access by matching the refractive index of the acrylic blades and casing with that of the working fluid, an aqueous solution of sodium iodide. Taking advantage of the resulting

[1]Corresponding author.

Contributed by the International Gas Turbine Institute (IGTI) of ASME for publication in the Journal of Turbomachinery. Manuscript received August 23, 2017; final manuscript received September 5, 2017; published online October 3, 2017. Editor: Kenneth Hall.

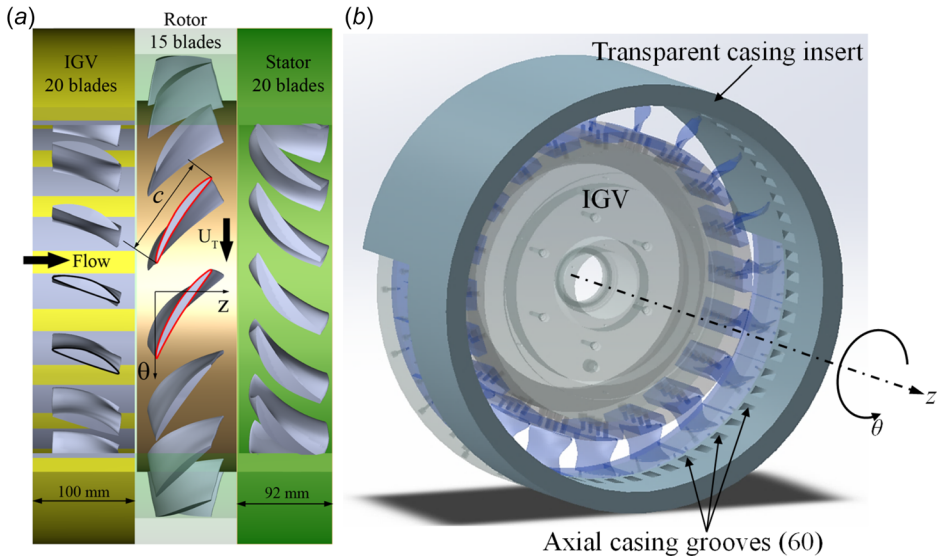

Fig. 1 (*a*) Configuration of the one and a half stages axial low speed fan and (*b*) a perspective view of the IGV with ACGs

unobstructed optical access, previous studies have already examined tip clearance flows [22–26], and recent work [27–29] has focused on the machine described in the present paper, without casing grooves. In particular, Chen et al. [29] show that the onset of stall involves formation and propagation of a large-scale backflow vortex (BFV). They form radially inward from the TLV, at the interface between the swirling and jetting tip leakage flow and the main passage flow. Once formed, these structures propagate to the next passage either across the tip gap or upstream of the blade leading edge (LE).

To study the flow structure generated by ACGs, we have installed an acrylic ring containing axial casing grooves with geometry similar to that studied by Müller et al. [7]. Performance tests, qualitative flow visualization by cavitation, and quantitative SPIV measurements in multiple planes elucidate the flow in the tip region and within the casing grooves. As discussed below, performance tests show that the grooves cause substantial improvements in performance and delay the onset of stall. These improvements appear to be related to three effects: first, substantial fractions of the leakage flow and the TLV are entrained periodically into the groove, greatly reducing the TLV strength, and confining the TLV remnants to the downstream/entrance corner of the groove. Second, the grooves prevent the formation of backflow vortices that play a dominant role in the onset of stall in the untreated machine. Third, as the flow exiting from the grooves propagates back to the blade, it causes periodic variations of about 10 deg in the relative flow angle around the blade leading edge, presumably affecting the blade loading periodically.

Experimental Setup

As shown in Fig. 1(*a*), the one-and-half stages low speed axial fan consists of a 20-blade inlet guide vane (IGV), a 15-blade rotor, and a 20-blade stator. The blades are based on the low-speed axial compressor facility at NASA Glenn, but their aspect ratio is reduced to accommodate operation in a liquid facility [24,30]. Relevant geometrical parameters of this machine, which has the same rotor as that used in Ref. [29], and the wide tip clearance in Ref. [28] are listed in Table 1. The tip clearance, as measured directly from the PIV images, is slightly smaller than that reported in these papers, most likely due to slight differences in rotor eccentricity. The casing and the rotor blades are made of acrylic, whose refractive index is the same as that of the fluid, a 62–63% by weight aqueous solution of sodium iodide. The kinematic viscosity of this fluid is 1.1×10^{-6} m^2 s^{-1} [31], and its specific gravity is 1.8. As illustrated by the perspective view in Fig. 1(*b*), the casing grooves are machined in an acrylic ring that surrounds the three blade rows. The groove dimensions, location, and orientation are shown in Fig. 2, and/or Table 1. The semicircular grooves have a diameter of $0.65c_A$, out of which, 33% overlaps with the rotor, and the rest extends upstream of the rotor. The evenly spaced, four-per-passage grooves are skewed by 45 deg in the positive circumferential direction, i.e., the same as the rotor rotation (Fig. 2(*b*)).

Detailed descriptions of the refractive index matched test loop can be found in Refs. [22–24]. Briefly, the fan speed is fixed at 480 RPM and the resulting Reynolds number based on the rotor chord length and tip speed is 1.07×10^6. The volumetric flow rate is measured by integrating the velocity profile obtained by translating a Pitot tube radially far downstream of the test section. The mean pressure rise across the machine is measured by a differential pressure transducer connected to pressure ports located upstream of the IGV and downstream of the stator. The performance is determined while operating the machine under the same conditions for several minutes, and results are based on averaging 200,000 points. The term performance refers to the pressure rise across the machines, and that the present study does not include measurements of efficiency. Cavitation resulting from running the facility at low mean pressure is used for visualizing vortical structures. The SPIV measurements are performed while keeping the facility at a much higher mean pressure to suppress all forms of cavitation.

Table 1 Stage-relevant geometrical parameters

Casing diameter, D (mm)	457.2
Hub radius, r_{hub} (mm)	182.9
Rotor passage height, L (mm)	45.7
Rotor diameter, D_R (mm)	453.6
Rotor blade chord, c (mm)	102.6
Rotor blade span, H (mm)	43.9
Rotor blade stagger angle, γ (deg)	58.6
Rotor blade axial chord, c_A (mm)	53.5
Measured tip clearance, h (mm)	1.8 (0.0175c or 0.041H)
Axial casing groove diameter (mm)	34.8
Groove skew angle (deg)	45
Total number of grooves	60
Shaft speed, Ω (rad s^{-1}) {RPM}	50.27 {480}
Rotor blade tip speed, U_T (m s^{-1})	11.47
Reynolds number, $U_T c/\nu$	1.07×10^6

Optical setups used in this study are shown in Fig. 3. During cavitation visualizations, the tip region is illuminated by two continuous halogen lamps shown in Fig. 3(*a*). Images have been recorded by a PCO.dimax high-speed CMOS camera at 5760 frames/s, corresponding to 48 images per blade passage, at a resolution 960×792 pixels. The field of view is 143.6×118.5 mm^2. Index matching allows acquisition of PIV-based data in any desired plane. The setup for SPIV measurements in meridional planes is illustrated in Fig. 3(*b*). The flow field is seeded with 13 μm, silver-coated hollow glass spheres that have a specific gravity of 1.6, and illuminated by dual head, 200 mJ/pulse Nd:YAG laser expanded to a laser sheet thinner than 1 mm. The images are recorded by a pair of Imperx B6640 CCD cameras that have 6600×4400 pixel arrays. The total field of view is 44.9×41.1 mm^2, and the delay between exposures is 20 μs. Imaging conditions are satisfied by inclining the lenses by the Scheimpflug angles. Observations are performed through acrylic prisms whose surfaces are perpendicular to the lens axes. Data have been recorded in three equally spaced circumferential angles separated by $\Delta\theta = 1.5$ deg, which are labeled as θ_1, θ_2, and θ_3. Angles θ_1 and θ_3 are located close to the inside edges of a casing groove without cutting through them. Angle θ_2 cuts the entrance to the groove. As shown in Fig. 3(*c*), SPIV measurements have also been performed at a (z, θ) plane, where the radially outer edge of the laser sheet coincides with the blade tip ($r^* = 0.96$). In this case, the images are recorded by a pair of 2048×2048 pixels, PCO.2000 cameras, also using exposure intervals of 20 μs, and the field of view is 40.2×52.2 mm^2. To complete the picture, especially unsteady flow features, time-resolved two-dimensional (2D) PIV measurements at 2.4 kHz have been performed in a plane that is nearly parallel to the center plane of the grooves (Fig. 3(*d*)). In this case, the image pairs have been recorded by the PCO.dimax camera, at a resolution of 864×892 pixels, uses frame straddling to achieve an in-pair delay of 40 μs.

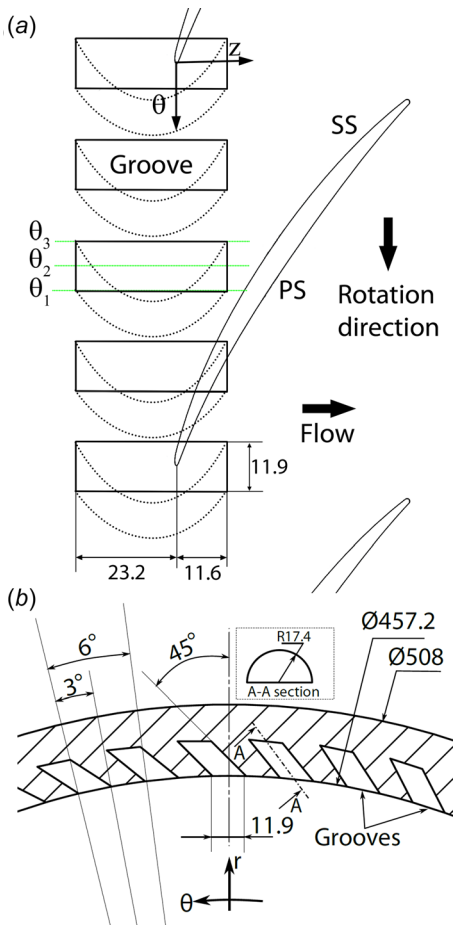

Fig. 2 The ACG configuration: (*a*) radial view and (*b*) streamwise view (looking upstream). All dimensions are in mm.

Following Wieneke [32], two steps are used for calibrating the SPIV images. Coarse calibration is performed by raising the entire camera and illumination system vertically as a unit and translating a dotted target immersed in a box filled with the same fluid. Subsequently, the system is lowered, and the so-called fine-resolution self-calibration is performed in the actual sample area. Preprocessing of the images consists of background subtraction [33], followed by contrast enhancement using a modified histogram equalization algorithm described in Ref. [34]. The FFT-based commercial PIV package, LaVison DaVis, is used for multipass cross-correlation of the image pairs. For the meridional planes, the final interrogation window size is 32×32 pixels, and with 50% overlap, achieves a vector spacing of 0.137 mm. For the (z, θ) plane, the final window size is 24×24 pixels, providing a vector spacing of 0.214 mm with 50% overlap. For the 2D data, the final window size is 32×32 pixels, and using 75% overlap, the vector spacing is 0.345 mm. The data are postprocessed by a universal outlier detection algorithm [35] that rejects spurious vectors. Based on our previous studies [23], the uncertainty in instantaneous velocity is about 0.1 pixel, corresponding to 0.4–0.8% of the tip speed, provided there are more than five particles in each interrogation window. The uncertainty in ensemble-averaged velocity is at least an order of magnitude smaller.

Data are presented in a cylindrical coordinate system (r, θ, z) whose origin is located at the center of the fan and coincides with the blade tip leading edge. The corresponding instantaneous velocity components are u_r, u_θ, and u_z, and the rotor rotates in the positive circumferential direction. The normalized radial coordinate, defined as $r^* = (r - r_{\text{hub}})/L$, is used throughout this paper. At least 2500 instantaneous realizations are obtained for every setup and rotor blade orientation (termed phase). Ensemble-averaged velocity components, denoted as U_i, are calculated by averaging all the data obtained for each phase. Velocity fluctuations are defined by $u_i' = u_i - U_i$, i.e., by deviation of the instantaneous data from the ensemble-averaged result. The orientation/phase of the blade relative to the groove is represented by the blade chord fraction (s/c) that the θ_2 plane (Figs. 2 and 3) intersects the blade chord. For clarity, $s/c = 0$ represents the phase where θ_2 is aligned with the blade LE. The SPIV data have been recorded at 14 different phases, covering an entire blade passage, but the planes are not distributed evenly, with finer separation of $\Delta s/c = 0.055$ around the leading edge, and coarser spacing, $\Delta s/c = 0.11$ for high chord fractions.

Results and Discussion

Effects of ACGs on the Performance. The performance curves with and without casing grooves are compared in Fig. 4. The flow coefficient is defined by $\varphi = V_Z/U_T$, where V_Z is the volumetric flow rate divided by the annular area of the rotor passage. The pressure coefficient is $\psi_{SS} = (P_{\text{exit}} - P_{\text{in}})/0.5\rho U_T{}^2$, where $P_{\text{exit}} - P_{\text{in}}$ is the pressure difference across the entire machine. At high flow rates, the grooves cause a slight decrease in pressure rise. However, for most of the measured range, they improve the performance substantially, by as much as 17% at $\varphi \sim 0.25$. Furthermore, while the onset of stall in the untreated machine occurs at $\varphi \sim 0.24$ [29], stall does not occur in the grooved case until $\varphi < 0.15$, where the performance drops rapidly. For both cases, the rapid decline in performance is accompanied by an audible increase in vibration-induced noise. Hence, the axial grooves reduce the flow rate at the onset of stall by 40%.

Visualization of Flow Structures by Cavitation. Figure 5 shows sample images of cavitation at two different flow rates comparing the TLV structure with a smooth casing to that developing when the ACGs are installed. The blade tip profiles and

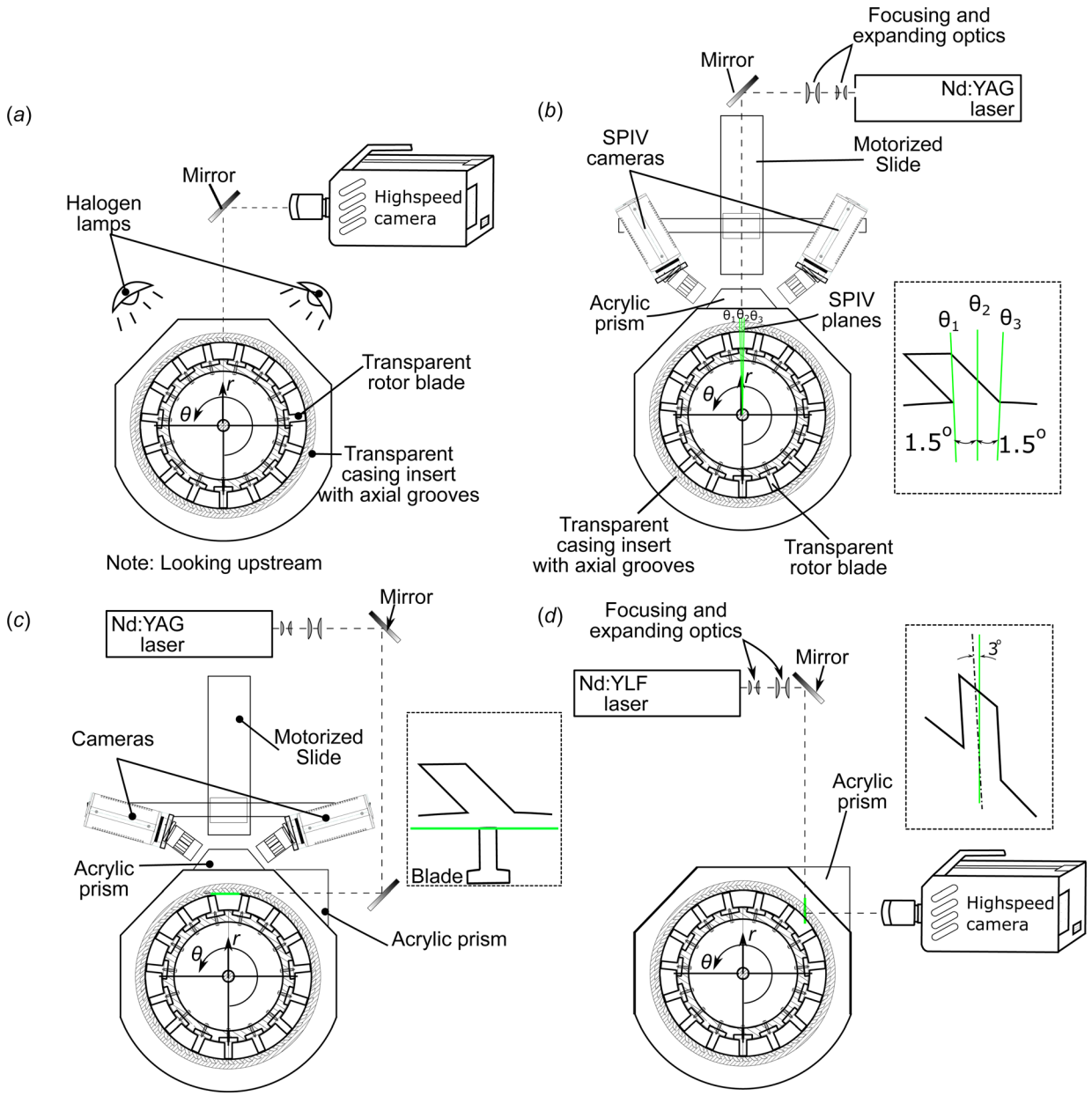

Fig. 3 Experimental setups for: (*a*) cavitation flow visualization, (*b*) SPIV in three meridional planes, (*c*) SPIV in a (z, θ) plane intersecting the blade tip at $r^* = 0.96$, and (*d*) 2D time-resolved PIV inside a groove

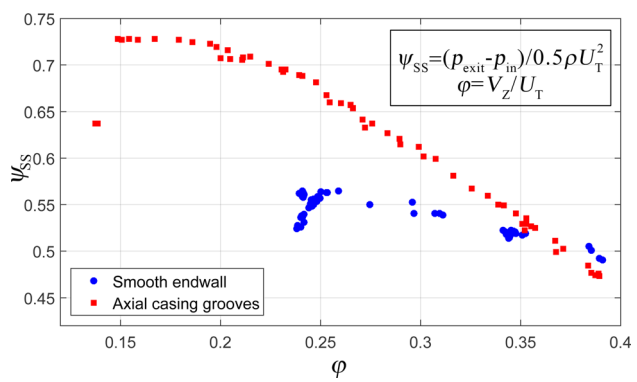

Fig. 4 Performance curves for $h/c = 1.8\%$, with and without the ACGs

locations of the grooves are highlighted for clarity. At $\varphi = 0.35$, when the performance of the two machines is not substantially different, Figs. 5(*a*) and 5(*b*) represent a phase for which one of the grooves is located above the initial rollup point of the TLV in the untreated case. The presence of tip leakage cavitation (see annotations) indicates that there is a leakage flow in both cases. However, the point where a distinct TLV first appears on the suction side (SS) is located further along the blade in the grooved endwall.

Further downstream, the TLV in the untreated rotor gradually detaches from the blade, and small-scale BFVs aligned perpendicularly to the blade begin to form between the SS corner and the TLV (marked as BFV). The mechanisms generating them and their influence on the onset of stall are the focuses of our previous publication [29]. For the treated endwall (Fig. 5(*b*)), the TLV also begins to migrate away from the blade between the first and the middle grooves (bottom and middle grooves in Fig. 5(*b*)). Yet, near the middle groove, the TLV becomes confined to the space between this groove and the blade, resulting in kinks in the TLV

trajectory on both sides of this groove. Further downstream, where the aft parts of the blade are not located under the grooves, the TLV detaches from the blade again, and several BFVs start to appear as well.

At $\varphi = 0.25$, the prestall condition of the untreated endwall, the TLV rolls up near the blade leading edge, and migrates away from the SS at a shallow angle with the circumferential direction. The cavitation disappears at midpassage, as the vortex breaks up under the influence of the BFVs that appear intermittently in the middle of the rotor passage (e.g., Fig. 5(*c*)). As discussed in Ref. [29], the formation and circumferential propagation of the BFVs diagonally upstream, and their penetration across the tip gap or around the leading edge of the next blade triggers generation of similar structures in the next passage, and so on. The BFV vorticity is originated from the leakage flow, but it rolls up radially inward from the TLV. As the BFV crosses the tip gap, the TLV rollup is disrupted, and in some cases, pushed further along the blade briefly, suggesting a temporary reduction in the local blade loading. This process is intermittent under prestall conditions, but is a major contributor to the substantial increase in turbulence level over a broad area. At the onset of stall (e.g., at $\varphi = 0.24$), the BFVs roll up earlier, and appear more frequently, sometimes more than one per passage. They also grow more rapidly and to a larger size. Once formed, their propagation from one passage to the next persists for a while. Furthermore, they appear to rotate with the blade, while migrating slowly downstream, indicating that the flow of the entire tip region is nearly blocked. Hence, generation and circumferential propagation of the BFVs is a primary phenomenon associated with the onset of stall.

For the grooved endwall and $\varphi = 0.25$, Fig. 5(*d*) shows that the TLV boundary becomes wavy, with what appears to be a narrower waist under the first groove combined with decreased tip leakage cavitation in the same area. The high-speed movies show that the waist is formed as part of the TLV cavitation is entrained into the groove. Further away from the blade, the TLV tail seems to diminish under the middle groove, leaving very little cavitation beyond it. As demonstrated quantitatively later, this phenomenon is caused by entrainment of substantial parts of the TLV into this groove, leaving limited amount of circulation in the main channel. Most importantly, however, is the disappearance of the BFVs, both large and small ones. Hence, the grooves eliminate or at least greatly suppress the primary flow phenomenon propagating circumferentially from one blade passage to the next under prestall and stall conditions in the untreated passage. Both effects, namely the periodic suction of TLV and elimination of the BFVs, persist at flow rates much lower than $\varphi = 0.25$ (not shown). Once stall occurs at $\varphi < 0.15$, the TLV disappears completely periodically, indicating a broad loss of blade loading over more than one blade passage at a time. We have not focused on this domain fearing for the ability of the blades to withstand the unsteady loading for extended periods.

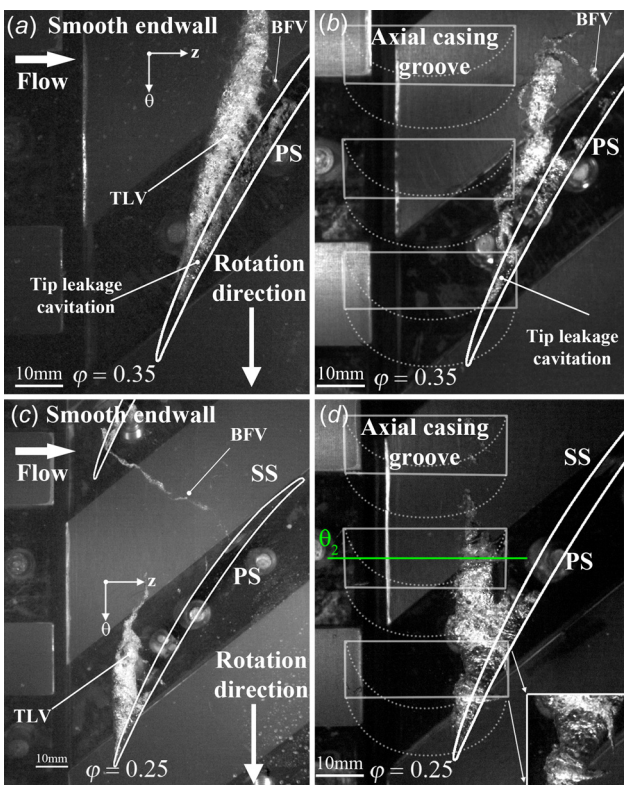

Fig. 5 Sample cavitation images showing vortical structures in the rotor passage without (left column) and with ACG (right column). Top row (*a*) and (*b*): $\varphi = 0.35$, and bottom row (*c*) and (*d*): $\varphi = 0.25$. Entrances to the grooves are indicated by solid gray lines, and their outlines are marked by dashed lines. Insert in (*d*) is a magnified view of the groove corner.

Flow Characteristics in the (z, θ) Plane. All the PIV data presented in this paper have been acquired at $\varphi = 0.25$ in order to focus on mechanism preventing the onset of stall. Figure 6 shows six superpositions of ensemble-averaged in-plane velocity vector fields and contours of U_r in a (z, θ) plane intersecting the blade tip. The field of view contains two grooves, and their locations are highlighted, along with the location of the three meridional planes (θ_1, θ_2, and θ_3) discussed subsequently. The selected phases elucidate the impact of the grooves on the flow around the blade tip, including the vicinity of the TLV. Corresponding cavitation images for two phases, $s/c = 0.22$ and 0.33, based on the location of θ_2 are provided in Fig. 7 for comparison. Several trends are evident:

(i) Consistent with Ref. [29], there is generally an inflow into the groove on the downstream side, which overlaps with the blade, and outflow from the groove on the upstream side. The magnitudes and distributions of inflow and outflow vary spatially and temporally, depending on the orientation of the blade relative to the grooves. Starting with the blade effect, $U_r > 0$ along the pressure side (PS) of the blade, as expected. Furthermore, U_r transitions from positive to negative values along the TLV center on the SS, making this transition a convenient qualitative means of identifying the trajectory of the TLV center. A comparison to Fig. 7 shows that the upstream edge of the narrow negative U_r area nearly coincides with the upstream edge of the TLV cavitation, confirming that the positive and negative U_r layers correspond to the TLV-induced velocity. In addition, the measurements in meridional planes discussed later confirm that the transition in U_r sign corresponds to the TLV center.

(ii) Except for periods when the downstream end of the groove is facing the SS of the blade (e.g., Fig. 6(*c*)) and strongly affected by the TLV, U_r is largely positive at the downstream end (the inflow/entrance end) of both grooves. This radial inflow, combined with $U_\theta > 0$ consistent with the groove angle, increases when the entrance is aligned with the PS of the blade. Such an increase occurs, e.g., when the LE is aligned with θ_2 ($s/c = 0$) in Fig. 6(*a*), or when the LE is aligned with the lower groove at $s/c = 0.33$ (Fig. 6(*c*)). The magnitude of U_r peaks as the PS approaches the downstream edge of the upper groove in Fig. 6(*b*) and the lower groove in Fig. 6(*d*).

(iii) $U_r < 0$ over the entire upstream/exit end of the grooves, with the exit flow being persistently higher at the high θ corner of the grooves, e.g., the corner corresponding to θ_1 in the upper one.

(iv) Discontinuities in the TLV trajectory. When the blade SS is facing the entrance to the groove, Fig. 6(*c*) shows that

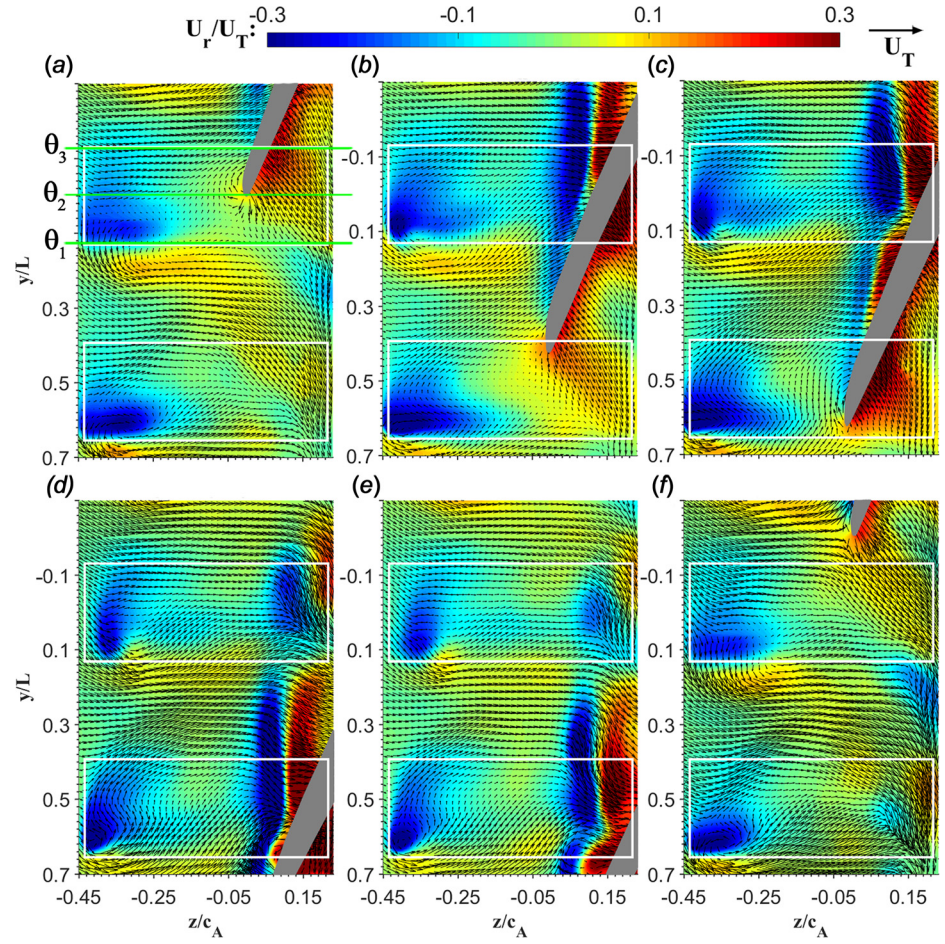

Fig. 6 Ensemble-averaged in-plane velocity vectors (nearly U_z, U_θ) superimposed on contours of the radial velocity component ($r^* = 0.96$). Vectors are diluted by 4:1 in both directions for clarity. The values of s/c indicate the intersection of the θ_2 plane with the blade chord: (*a*) $s/c = 0$, (*b*) $s/c = 0.22$, (*c*) $s/c = 0.33$, (*d*) $s/c = 0.55$, (*e*) $s/c = 0.66$, and (*f*) $s/c = 0.98$.

the TLV signature is divided into two parts, consistent with the corresponding cavitation images (Fig. 7(*b*)). The first part extends from the LE to vicinity of θ_1. It is characterized by a TLV confined to the vicinity of the blade SS with a weak vortex-induced velocity. The second part originates from the region facing the groove entrance, close to the SS surface, where the in-plane flow appears to converge toward this origin. The (positive and negative) TLV-induced velocity is initially quite high, reaching 30% of the tip speed, and the vortex center remains aligned in the circumferential direction, not far from the downstream edge of the groove. As the SS moves away from this groove, e.g., in Figs. 6(*d*) and 6(*e*), the remnants of the TLV-induced radial velocity decrease in magnitude, but remain "latched" to the downstream corner of the groove. As demonstrated below, the decreasing TLV signature is associated with partial entrainment of the TLV into the groove. These decaying TLV remnants finally disappear in Fig. 6(*f*), only as the entrance to the groove begins to be influenced by the PS of the next blade and associated increase in radial inflow. Essentially, the same phenomenon occurs around the downstream end of the lower groove, resulting in two TLV discontinuities in Fig. 6(*d*). These grooves are located at different circumferential angles relative to the location of the IGV blades, suggesting that the IGV or its wake is not playing primary roles in the observed phenomena.

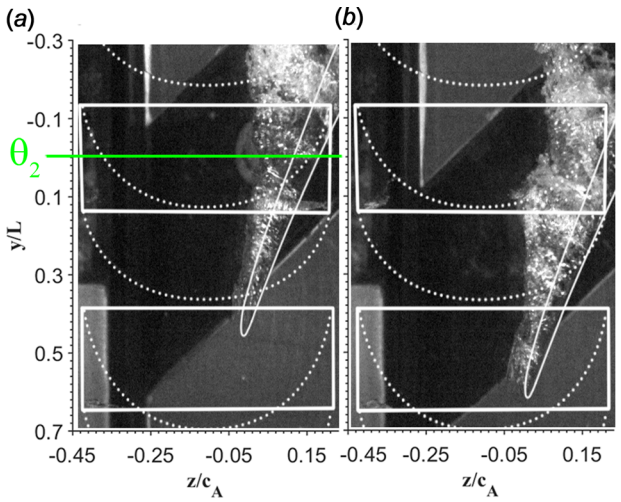

Fig. 7 Cavitation images at: (*a*) $s/c = 0.22$ and (*b*) $s/c = 0.33$

(v) The distribution of in-plane velocity components (U_z,U_θ) vary substantially with blade orientation relative to the groove but persistently show the stream originating from the exit and propagating diagonally toward the blade with $U_\theta < 0$ and $U_z > 0$. As shown later, this stream causes fluctuations in the relative flow angle around the blade LE. The direction of U_θ is negative in most of the area

overlapping with the groove, as expected, but transitions rapidly to positive values near the θ_1 corner, followed by a sharp turn toward the axial direction. The latter phenomenon is likely caused by the main passage flow circumventing the jet exiting from the groove.

Flow Characteristics in the Meridional Planes. Figure 8 provides two samples of the instantaneous vectors of the in-plane velocity components and contours of the plane-normal vorticity in the center plane of the groove for different *s/c*. In both cases, the flow circulates in the groove, entering from the downstream side and exiting from the upstream side, as already observed in prior numerical studies [10]. The time-resolved data recorded in this plane clearly show that the flow always circulated in the groove in the same direction, but the velocity magnitude and flow direction around the downstream/entrance end vary substantially with blade location relative to the groove. At $s/c = 0.22$ (Fig. 8(*a*)), when the blade PS is exposed to the downstream end of the groove (see Fig. 6(*b*)), the inflow is dominated by a strong narrow jet originating from the PS. Conversely, at $s/c = 0.44$ (Fig. 8(*b*)), when the blade SS is already located downstream of the groove, the tip leakage flow seen on the bottom right corner of the plot is mostly axial. This axial flow persists for about 20% of the groove's length, and then turns into the groove as a diagonal jet while causing flow separation at the downstream corner. As discussed below, the positive vorticity at the upstream side of the jet is originated from the TLV, and the negative vorticity on the downstream boundary is originated from the enwall boundary layer. It is also evident that

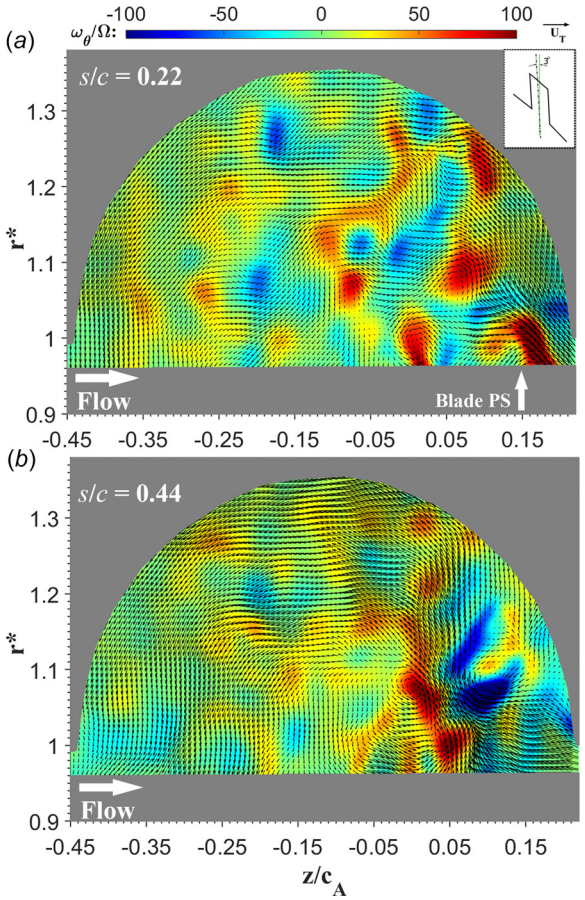

Fig. 8 Samples of instantaneous vectors of in-plane velocity components and contours of plane-normal vorticity in the center plane of the groove. (*a*) *s/c* = 0.22, when the blade PS is exposed to the groove, and (*b*) *s/c* = 0.44, when the SS is located downstream of the groove.

the peak vorticity in entrained vortical structures persistently decreases as the flow circulates in the slot. Furthermore, the organized vortical layers at the entrance are replaced with what appears to be "scrambled" turbulence at the exit.

Figures 9–11 display the distributions of ensemble-averaged circumferential vorticity and three velocity components for three different *s/c* selected to represent different phases of blade–groove interactions. Each figure displays data for three meridional planes intersecting the same groove at different location, as illustrated in the top right hand corner. Inherent to variations in their location relative to the groove, the flow structures displayed in them differ significantly. The following discussion highlights and analyzes some of the main features, but not all of them. Yet, we opt to present the entire sets for the selected *s/c* (data are available for other regions as well) to give the reader a complete picture on the blade–groove interactions. The datasets are shown as follows.

General Persistent Features. The discussion starts with features that persist at all *s/c*. First, consistent with Fig. 6, the outflow from the upstream end of the groove peaks close to the θ_1 plane irrespective of blade orientation, with U_r reaching 40% of the tip speed. The corresponding peak negative values of U_θ are systematically lower, i.e., the returning flow is not skewed at the same angle as the groove even before entering the passage. A much weaker outflow is also evident in all the θ_2 (middle) planes. As the radially inward jet penetrates the passage, it creates a region with U_z deficit bounded by a negative $<\omega_\theta>$ layer upstream. Second, at θ_1, a narrow positive vorticity layer aligned along $r^* \sim 1$ extends along the boundary of the groove, except for the upstream and downstream corners. Being located near the edge of the groove, this layer is originated from the nearby endwall boundary layer, as the corresponding sharp transition in U_z confirms. Third, consistent with the skew angle, the inflow into the groove (downstream side) largely involves regions with positive radial and circumferential velocity components. However, the flow phenomena there are complex and phase-dependent due to the blade and TLV interactions with the groove discussed below.

Phase-Dependent Flow Features. Figure 9 corresponds to $s/c = 0.22$, the same orientation as Figs. 6(*b*) and 7(*a*), providing multiple viewing angles on the same phase. Here, part of the blade PS, which includes the θ_1 and θ_2 planes, is exposed to the downstream corner of the groove, resulting in a high-speed jetting inflow, with radial velocity well above 50% of the tip speed. The circumferential velocity is much smaller, indicating, like in the exit, that the inflow is not aligned with the groove skewness. In the θ_1 plane, a small TLV is already rolled up near the SS tip corner, but substantial fraction of the vorticity is concentrated above the blade tip. In the θ_2 plane, which corresponds to the origin of the second part of the TLV and where the vortex is "discontinuous," the vorticity is mostly confined to the blade tip. At the end of the groove, in the θ_3 plane, the distinct vortex reappears. These observations suggest that the TLV discontinuity occurs as inflow separates in the PS corner, and jets straight into the groove, with substantial fraction of the vorticity originating from the PS boundary layer remaining above the blade tip (a comparison to the untreated case follows). Also notable for this phase is the wide layer with negative U_θ in the θ_1 plane, just below $r^* \sim 1$. As Fig. 6(*b*) demonstrates, this phenomenon is originated from the outflow from the next (lower) groove, and as discussed later, causes periodic variations in the relative flow angle around the blade LE.

At $s/c = 0.33$ (Fig. 10), which corresponds to Figs. 6(*c*) and 7(*b*), the TLV is split in the θ_1 plane, as part of it is entrained into the groove by the narrow but fast radial jet ($U_r/U_T > 0.6$) still originating from the PS. The abovementioned wide layer with $U_\theta < 0$ at $r^* \leq 1$ originating from the neighboring groove is evident in this plane as well. In the θ_2 plane, the PS is no longer exposed to the groove, the high-speed tip leakage flow becomes predominantly axial with U_z exceeding 60% of the tip speed, and the radial

flow into the groove diminishes. Flow separation occurs at the corner of the groove, near the SS tip, creating a pair of counter-rotating vortices, one associated/coinciding with the TLV, and the other occupying the corner with the vorticity originating from the endwall boundary layer. In the θ_3 plane, a distinct TLV is already detached from the blade, and a shear layer with the same vorticity sign, seen also in all the untreated cases [28], connects it to the SS tip corner. The circumferential velocity around the vortex center is positive and higher than the surrounding area, i.e., the TLV behaves like a swirling jet. A negative vorticity layer extends from the endwall upstream of the TLV. A similar layer forms in untreated tip flows [28], where the vorticity is originating from the endwall boundary layer, above the blade tip, and separates from the wall at the point where the main passage flow meets the backward tip leakage flow.

At $s/c = 0.55$ (Fig. 11), which corresponds to Fig. 6(*d*), the blade SS is located just to the right of the present field of view. There are two vortices near the downstream/entrance corner of the groove in the θ_1 plane. The first is latched to the corner and the second is a small, concentrated, and recently rolled-up vortex located near the blade SS. In the θ_2 plane, these two structures are already merged into a larger single vortex with low peak vorticity centered slightly upstream of the groove corner. The location of this vortex remnants just upstream of the corner is consistent with the cavitation images and the (z, θ) plane data. The leakage flow with negative U_z along the endwall and the upper part of the vortex turns upward and becomes a diagonal jet at the entrance to the groove. It carries with it positive vorticity originating from the blade (or TLV) and negative vorticity originating from the endwall boundary layer. Yet, the negative axial velocity (Fig. 11(*h*)) and elevated circumferential velocity (Fig. 11(*k*)) in this area, the latter implying a reduced velocity relative to the blade, indicate that the TLV is still powerful enough to block part of the passage flow. As discussed before, in the untreated endwall, the radial gradients of circumferential velocity at the bottom of the elevated U_θ region are involved in the formation and propagation of BFVs at the onset of stall [29]. As proposed below, one of the effects of the axial casing grooves is to confine the area with elevated U_θ to the immediate vicinity of the downstream corner of the grooves, preventing the formation of large BFVs that extend across the passage.

Finally, in the θ_3 plane, the TLV becomes distinct again and its peak vorticity is higher than that measured in the middle of the groove (Fig. 11(*c*)). The circumferential velocity in this area is also very high (Fig. 11(*i*)), implying that the TLV behaves like a swirling jet. At higher s/c (not shown), as the flow begins to be influenced by the PS of the next blade, the peak vorticity and circumferential velocity in this plane also diminish. It appears that the last remnants of the vortex latched to the corner are entrained into the groove.

To show the impact of vorticity entrainment on the TLV strength, Fig. 12(*a*) shows the evolution of the total positive

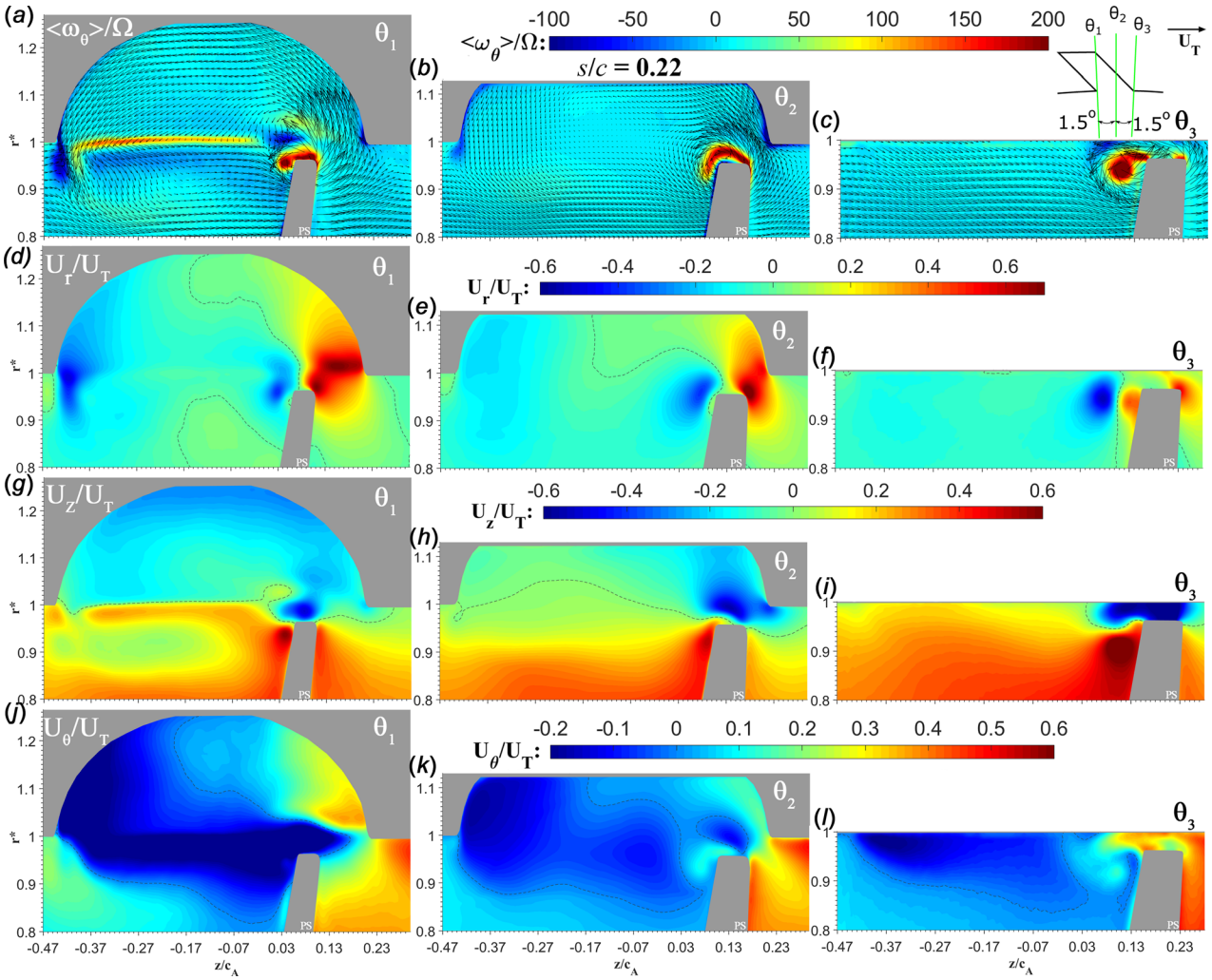

Fig. 9 Ensemble-averaged vorticity and velocity distributions in meridional planes θ_1 (left column), θ_2 (middle column), and θ_3 (right column) when θ_2 intersects the blade at $s/c = 0.22$. Top row: $<\omega_\theta>/\Omega$; second row: U_r/U_T; third row: U_z/U_T and bottom row: U_θ/U_T. Vectors are diluted by 5:1 in both directions for clarity in the top row. Dash lines indicate the zero values.

circulation on the SS of the blade, which is calculated by integrating the circumferential vorticity over areas where it is positive. The dashed lines correspond to the region where the blade is outside of the field of view; hence, part of the total circulation is not accounted for in the integration. Figure 12(*b*) shows the TLV circulation obtained in a similar integration, but only over areas restricted to the TLV. The vortex boundary is defined as the points where the vorticity drops to 10% of its peak value. Trends are compared to those of the untreated endwall. As is evident and expected, in the untreated case, the TLV and total circulation increase monotonically with *s*/*c*. The treated endwall has a higher circulation than the untreated casing at low *s*/*c*, in accordance with the higher pressure rise (Fig. 4) at the same flow rate. However, in the treated endwall, the circulation peaks at midchord and then decreases to low values in the aft part. This trend confirms quantitatively that interaction with the groove reduces the TLV strength, presumably by entrainment of part of the TLV circulation as the SPIV data demonstrate. To explain the observed trends, one should note that the magnitude of circulation is affected by two main effects, namely shedding from the blade, which increases the circulation, and entrainment by the groove, which reduces it. At low *s*/*c*, newly shed circulation appears to compensate for the entrained fraction. However, at midchord, the generation of new circulation weakens, as the minimal tip leakage cavitation confirms, and entrainment into the groove persists. Hence, the TLV circulation diminishes.

Discussion

The experimental data summarized in this paper provide intricate details on the effects of axial casing grooves on the flow structure in the tip region at $\varphi = 0.25$, which corresponds to pre-stall conditions in the untreated case. This section focuses on certain features believed to play an important role in the suppression of stall and the associated substantial increase in pressure coefficient. The discussion is based on comparisons to the flow structure near the untreated endwall. The grooves periodically entrain parts of the TLV circulation, limiting the vortex size and strength, and confining its remnants to downstream corner of the groove. By the time the leading edge of next blade arrives, the signature of the vortex latched to the corner essentially vanishes.

It should be noted that the present measurements enable us to determine that vorticity shed from the blade up to $s/c \sim 0.66$ is entrained into the groove. However, as the axial distance between SS of the blade and the groove increases, a TLV that is not entrained might rollup between the SS and the groove, outside of the present field of view. Such rollup occurs, e.g., at high flow rates, as Fig. 5(*b*) shows. However, Fig. 5(*d*) demonstrates that at

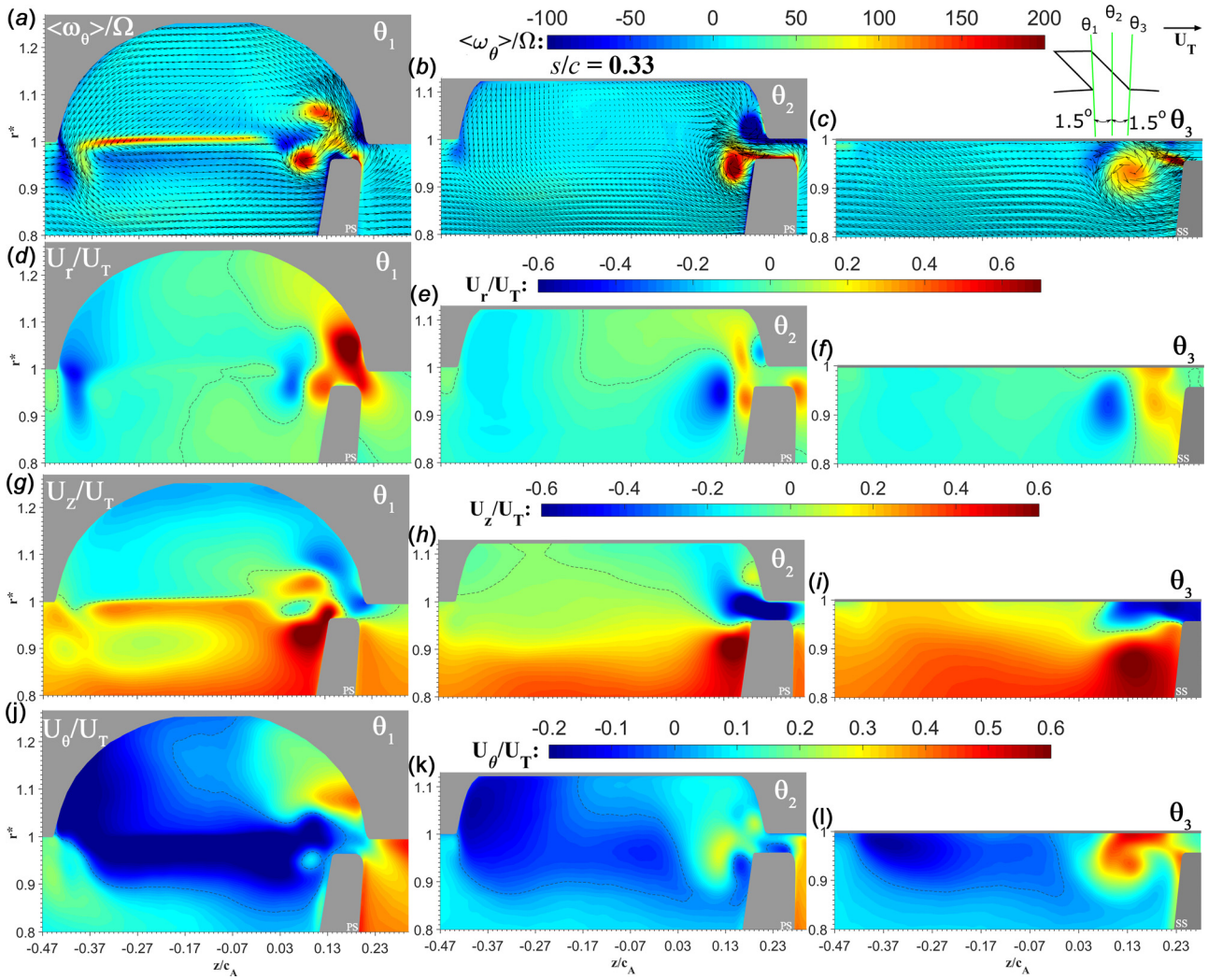

Fig. 10 Ensemble-averaged vorticity and velocity distributions in meridional planes θ_1 (left column), θ_2, (middle column), and θ_3 (right column) when θ_2 intersects the blade at $s/c = 0.33$. Top row: $\langle\omega_\theta\rangle/\Omega$; second row: U_r/U_T; third row: U_z/U_T and bottom row: U_θ/U_T.

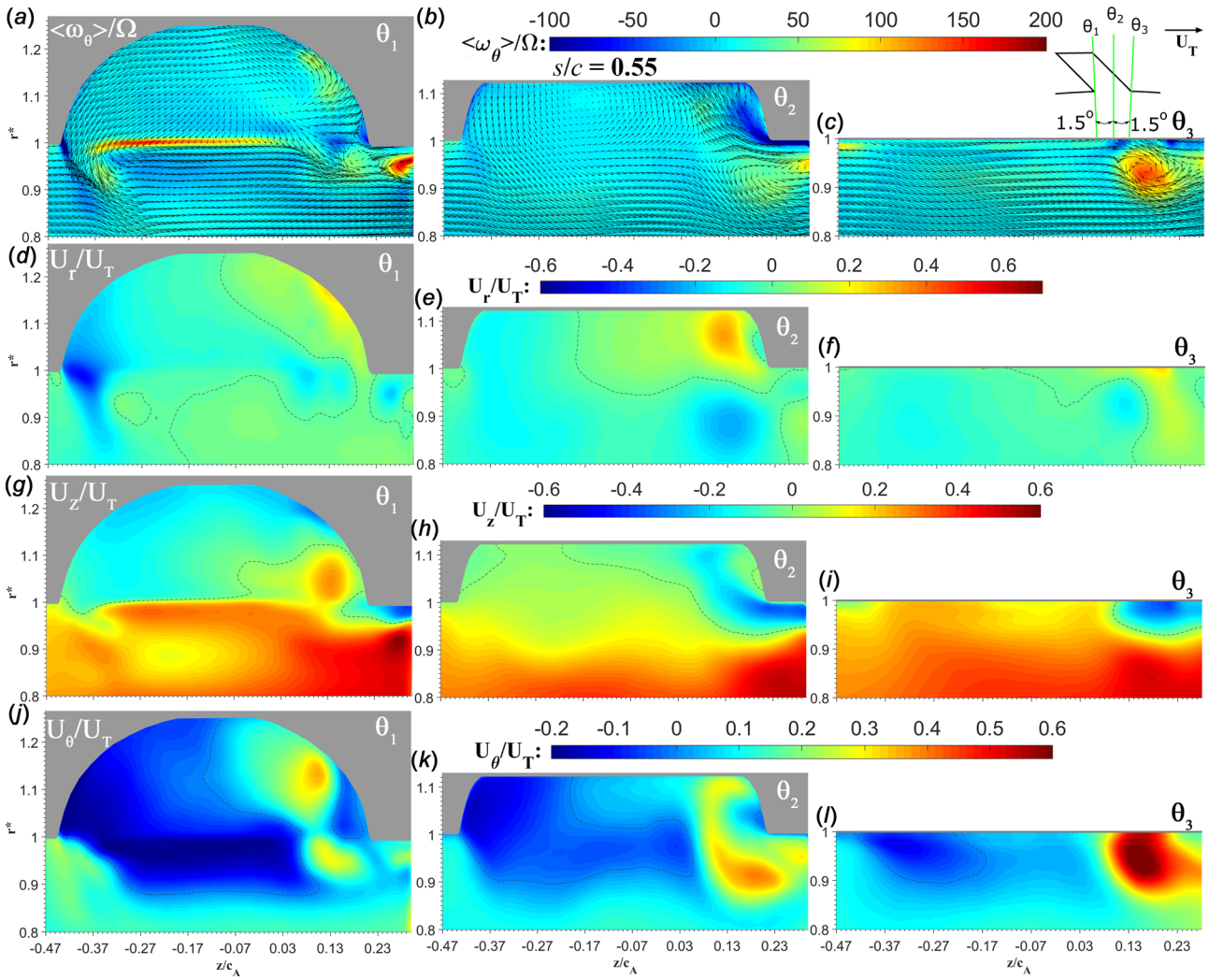

Fig. 11 Ensemble-averaged vorticity and velocity distributions in meridional planes θ_1 (left column), θ_2, (middle column), and θ_3 (right column) when θ_2 intersects the blade at $s/c = 0.55$. Top row: $<\omega_\theta>/\Omega$; second row: U_r/U_T; third row: U_z/U_T and bottom row: U_θ/U_T.

$\varphi = 0.25$, there is essentially no cavitation in the tip gap at $s/c > 0.5$, suggesting that the leakage flow in the aft part of the passage is weak, consistent with the rotor operating at a low flow rate. Furthermore, the movies do not show a cavitating vortex downstream of the groove, suggesting that if shed vorticity does roll up at $s/c > 0.66$, the resulting vortex is weak. Hence, it is reasonable to assume that most of the shed circulation remains within the field of view, and sucked into the grooves before the next blade arrives. In contrast, the strength of the ensemble-averaged TLV in the untreated machine increases monotonically with s/c (Ref. [28] and Fig. 12), eventually exceeding that of the treated machine in spite of the lower pressure coefficient. This vortex is initially aligned at a shallow angle to the circumferential direction (Ref. [29] and Fig. 5(*c*)), but the concentrated multiple vortex filaments comprising its center "break up" in the middle of the passage and scatter over a broad area [24,29]. Once, the TLV becomes fragmented, the area occupied by the scattered filaments grows rapidly, eventually reaching the PS of the next blade, but only at midchord. Hence, the onset of stall in the untreated rotor also does not involve direct interaction of the TLV with the vicinity of the leading edge of next blade.

Instead, in Ref. [29], it is shown that the onset of stall in the untreated rotor involves formation of BFVs that extend diagonally upstream, from the SS midchord of one blade to the PS near the leading edge of the neighboring blade. They propagate to the next passage across the tip gap or around the blade LE. A sample image of a prestall BFV is shown in Fig. 5(*c*). Much larger structures that appear when the rotor is stalled are displayed in Ref. [29]. The BFVs essentially disappear in the treated rotor, as the

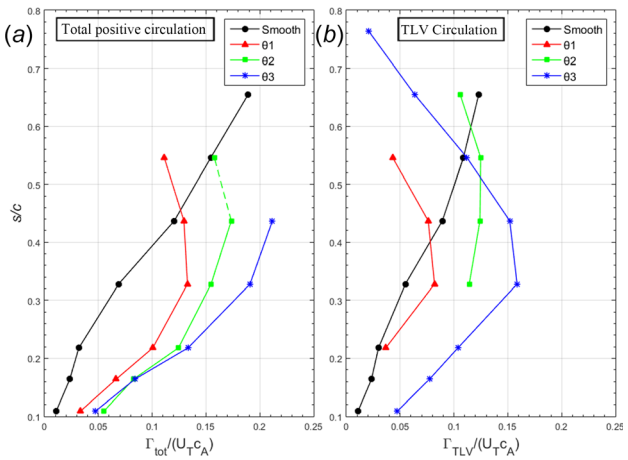

Fig. 12 Positive circulation: (*a*) over the entire blade SS and (*b*) in the TLV

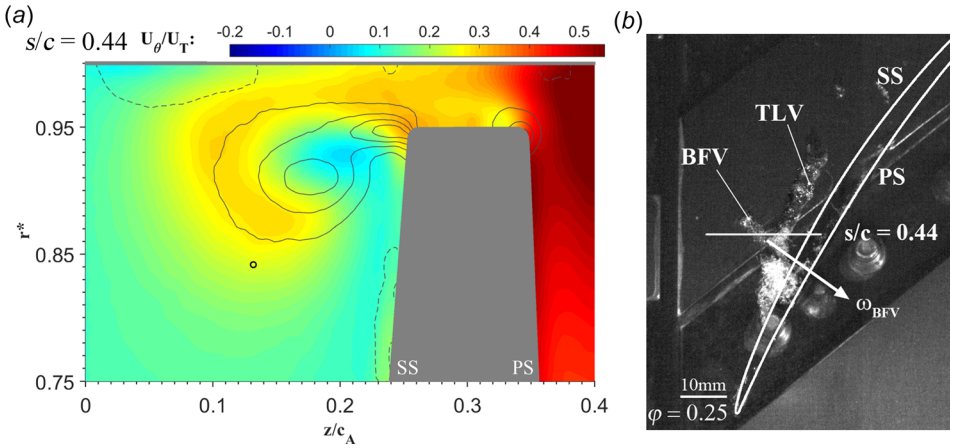

Fig. 13 (*a*) Contours of the distribution of U_θ at $s/c = 0.44$ and $\varphi = 0.25$ in the untreated rotor. The black lines are contours of circumferential vorticity. (*b*) A sample image shown an early phase of BFV formation at $s/c = 0.44$. The arrow shows the measured direction of ensemble-averaged vorticity at the point indicated in (*a*).

cavitation images and absence of their signature in the vorticity distributions under the TLV clearly indicate. To explain the reason for their disappearance, one must describe their origin briefly, summarizing the findings in Ref. [29]. As a visual aid, Fig. 13(*a*) shows the distribution of U_θ in the untreated passage at $s/c = 0.44$ and $\varphi = 0.25$. The layer of elevated U_θ is originated from the tip gap (and the PS) and surrounds the TLV center. The three-dimensional vorticity distribution, determined by recoding SPIV data in a series of closely spaced planes, indicates that the radial gradients in U_θ under the TLV, e.g., at the point marked in Fig. 13(*a*), are primary contributors to formation of a layer with elevated positive axial vorticity at this location. Similarly, a layer with negative radial vorticity is associated with the axial gradients in U_θ upstream of the TLV. Combined, they create a vortical "ring" originated from the tip gap that surrounds the TLV center. A similar ring has been observed around the TLV of an axial waterjet pump, so this phenomenon is not unique to the present machine [22]. Figure 13(*b*) is a sample image of a BFV located radially inward form the TLV during early phases of development. It also shows the *measured* direction of vorticity at the point marked in Fig. 13(*b*). As is evident, the BFV is parallel to the measured vorticity, confirming its origin, and both are nearly perpendicular to the TLV and the SS surface. The BFV rolls up into a distinct vortex when the vorticity layer is perturbed. As the TLV migrates away from the blade with increasing s/c, especially after it breaks up, the region of elevated U_θ expands to a substantial fraction of passage, eventually reaching the PS of the next blade. In fact, the high U_θ on the PS of the endwall in Fig. 13(*a*) is associated with the TLV of the previous blade. As a result, the BFVs also expand intermittently to the PS of the next blade (Fig. 5(*c*)), and then propagate across the tip gap or around the LE to the SS of this blade. Upon penetration, the BFVs delay the rollup of a TLV, increase the flow angle around the LE, and trigger generation of similar vortices in the next passage. Under stall conditions, the frequency and size of BFVs increase, and they regularly expand upstream of the leading edge of the next blade.

Admittedly, as Figs. 10(*k*) and 11(*k*) clearly show, regions with radial gradients in U_θ (and presumably axial vorticity) develop also under the TLV of the treated machine. Hence, BFVs could still form there. However, the grooves persistently limit the axial extent of this region, preventing the region with $\partial U_\theta/\partial r > 0$ from reaching the leading edge of the next blade. As a demonstration, Fig. 14 compares the distributions of U_θ at $s/c = -0.11$, a short distance ahead of the LE of the blade. Without the grooves (Fig. 14(*b*)), the elevated U_θ region extends well upstream of the blade LE ($z/c_A = 0$). Conversely, with the grooves, U_θ is near zero around the LE (Fig. 14(*a*)), and is negative in other phases (Figs. 9(*k*), 10(*k*), and 11(*k*)). There are two possible reasons for this effect: first, the high positive U_θ fluid is sucked periodically into the groove (Figs. 14(*a*) and 11(*k*)). Second, the flow direction

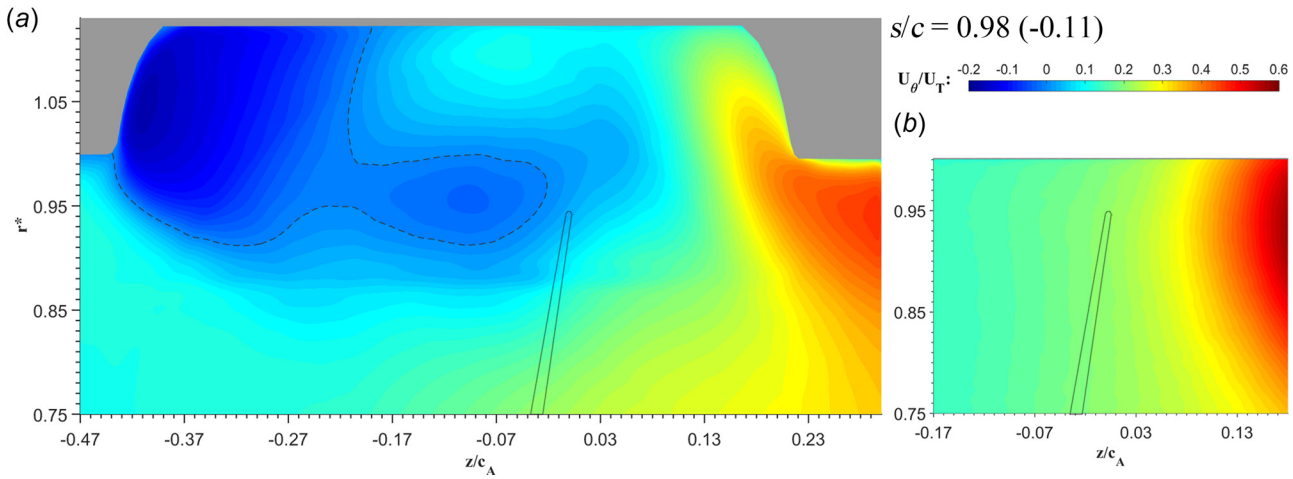

Fig. 14 Contours comparing the distribution of U_θ at $\varphi = 0.25$ and $s/c = -0.11$, i.e., upstream of the blade LE, in the: (*a*) rotor with ACGs and (*b*) untreated rotor. Dashed lines indicate the location of the blade LE at $s/c = 0.0$.

around the blade LE is influenced by the outflow from the grooves, where $U_\theta < 0$. In fact, all the (z, θ) vector maps in Fig. 6 show the diagonal "jet" exiting from the upstream end of the groove, and reaching the plane of the blade leading edge. Hence, while BFVs could roll up periodically in the $\partial U_\theta/\partial r > 0$ region, they could not propagate to the next passage. Interestingly, evidence of BFVs beginning to form can be seen in the cavitation images of the treated passage at $\varphi = 0.35$ (Fig. 5(*b*)) under the TLV segment located downstream of the grooves. Finally, Wilke and Kau [10] argue based on Reynolds-averaged Navier–Stokes simulations that the delay of stall in a compressor with axial grooves is associated with weakening of the TLV. In a way, the present results agree with this observation since the formation and growth of the BFVs appear to be direct outcomes of the tip leakage flow, as well as rollup, migration, and breakup of the TLV.

Comparisons between distributions of turbulent kinetic energy (TKE) could be used as statistical means of highlighting the effect on the flow stability of the TLV suction into the grooves in the treated rotor, and penetration of BFVs across the tip gap in the untreated machine. Figure 15 compares sample distributions of TKE defined as $k = 0.5(\overline{u_r'u_r'} + \overline{u_\theta'u_\theta'} + \overline{u_z'u_z'})$, where u_i' is the velocity fluctuation. In the tip region of the grooved endwall, the high turbulence is confined to the vicinity of the TLV (Figs. 15(*a*), 15(*c*), and 15(*e*)), and to the region of flow separation around the downstream corner of the groove (Fig. 15(*c*)). Once most of the TLV is sucked into the groove, at $s/c = 0.66$, the turbulence around the TLV remnants (Fig. 15(*e*)) is much lower than that near the center of the fragmented TLV after it breaks up in the untreated machine (Fig. 15(*f*)). Deeper within the groove, the TKE is substantially lower. Elevated turbulence levels, which are significantly lower than those at the entrance to the groove, develop also when the outflow from the groove interacts with the passage flow, as shown using different contour scales in the insert in Fig. 15(*a*). In other parts of the tip region, especially near the PS and entrance to the tip region, the TKE in the grooved machine is much lower than that in the smooth endwall. As demonstrated in Ref. [29], the high TKE near the PS and at the entrance to the untreated tip clearance (Figs. 15(*b*) and 15(*d*)) is dominated by the formation and penetration of the large BFVs across the tip gap. At higher flow rates, when the BFVs and fragmented TLV in the untreated machine do not make it to the PS of the neighboring blade, the turbulence at the entrance to tip gap is much lower.

The abovementioned periodic exposure to the outflow from the groove affects the flow direction near the leading edge of the blade, and presumably the blade loading. As illustrated in Fig. 16(*a*), in the present discussion, the relative flow angle is defined as the angle between the z-axis (positive axial direction) and the flow direction in the *blade reference frame*. Perpendicular views of the distribution of this angle are presented in Fig. 16. The insert in Fig. 16(*b*) also provides a reference distribution of this angle for a smooth endwall at the same blade orientation, with the dotted lines indicating the location of the LE. Figure 16(*a*) clearly shows that the outflow from the groove generates a layer with high flow angle, which propagates downstream and periodically increases the flow angle around the blade leading edge. The corresponding θ_1 and θ_2 planes (Figs. 16(*b*) and 16(*c*)) show the significant radial extent of this phenomenon. Evidently, the outflow from the grooves periodically increases the relative flow angle upstream of the LE by more than 5 deg. This increase does not appear to cause leading edge separation, at least for the present flow conditions.

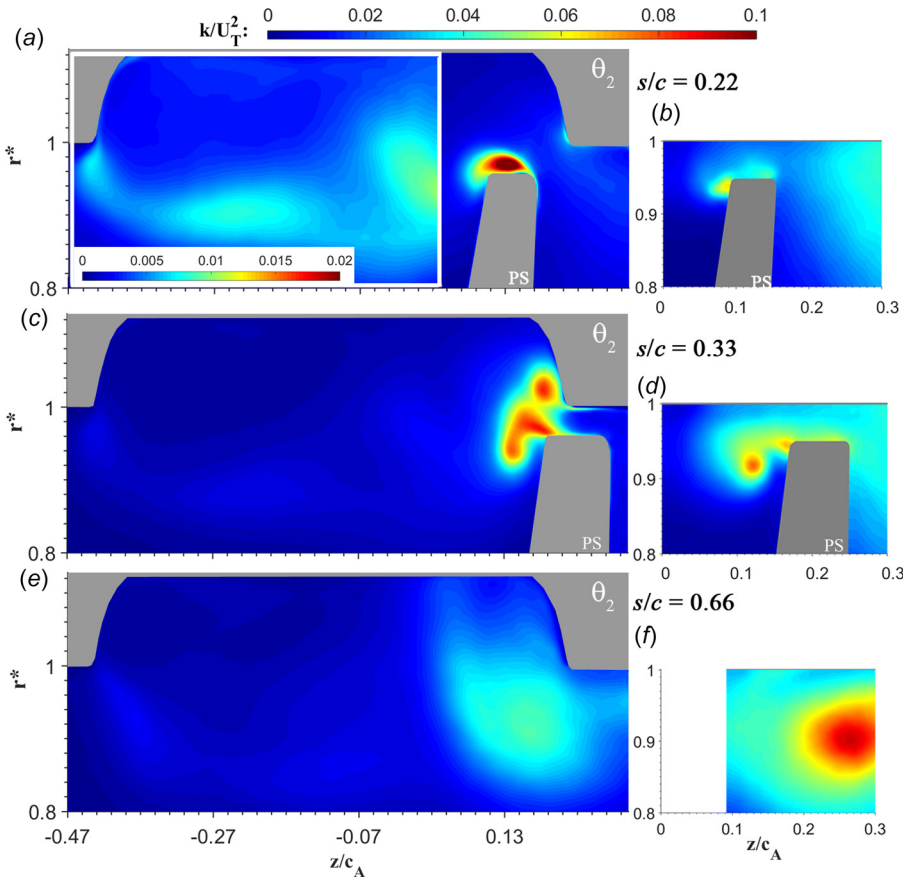

Fig. 15 Comparison of TKE distributions with casing grooves (left column) and smooth casing (right column): (*a*) and (*b*) $s/c = 0.22$, (*c*) and (*d*) $s/c = 0.33$, and (*e*) and (*f*) $s/c = 0.66$. Note the scale for the insert in (*a*) has a significant smaller range.

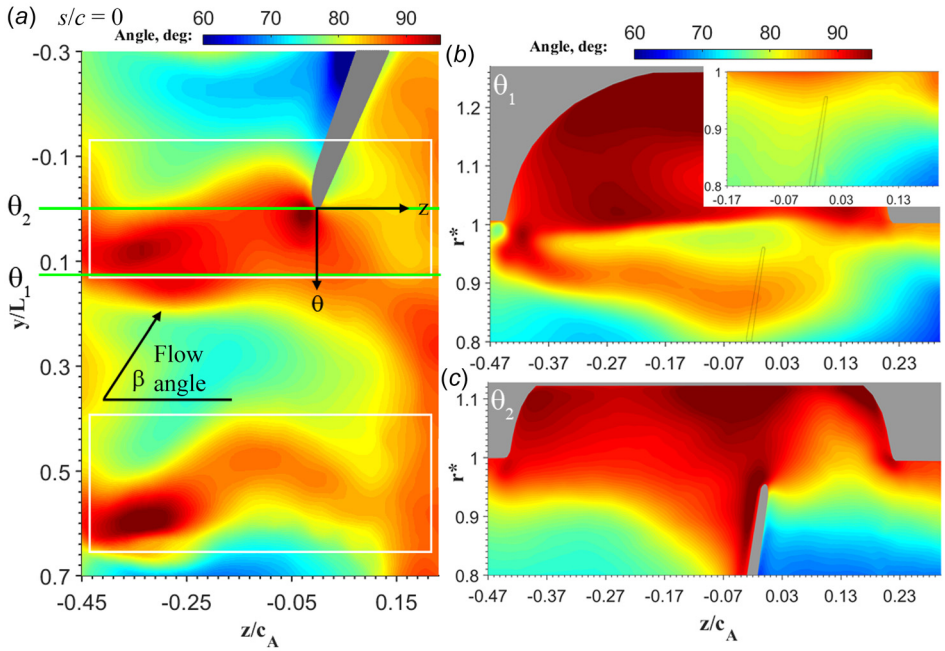

Fig. 16 Distribution of relative flow angles in the rotor reference frame. (*a*) (z, θ) plane at $r^* = 0.96$, (*b*) and (*c*) θ_1, θ_2 planes when the θ_2 plane is at $s/c = 0$. Insert in (*b*) shows the relative flow angle in θ_1 for the untreated case.

Conclusions

Performance tests, flow visualization, and PIV measurements confirm that axial casing grooves suppress the onset of stall in the tip region of an axial fan rotor and elucidate the flow mechanisms involved. Following Müller et al. [7], the semicircular grooves are skewed by 45 deg in the positive circumferential direction. There are four evenly spaced grooves in each rotor passage, with 33% of the groove overlapping with the rotor blade, and the rest extending upstream. Most of the present velocity measurements and flow visualizations are performed at a flow rate corresponding to pre-stall condition for the smooth endwall. The grooves reduce the stall flow rate by 40%, and cause substantial increase in pressure rise at low flow rates. Substantial improvements in stall margin are also reported in Ref. [7] for a transonic compressor. However, the grooves reduce the pressure rise at high flow rates. The reason for this performance degradation remains an open question that will be investigated in future experiments.

The velocity measurements show that a circulating flow enters the grooves at the downstream end and exits at the upstream edge, confirming prior results for axial casing grooves reported, e.g., by Smith and Cumpsty [5], Wilke and Kau [10], and Müller et al. [7]. The present measurements also show that the flow structure over the entire tip region and within the grooves, including the primary inflow location, varies periodically with blade orientation. The periodic outflow agrees with measurements performed by Takata and Tsukuda [4]. The inflow peaks when the downstream end of the groove is aligned with the PS of the blade, and decreases, but does not vanish, when this end is located near the SS. Flow separation occurs at the groove corners as the flow enters and leaves the groove, creating a secondary flow there, and suggesting that the groove geometry could be optimized further. The radially and circumferentially negative outflow is concentrated at the upstream corner of the groove. When this flow propagates to the blade leading edge, it causes a periodic increase in flow angle by as much as 5 deg. Yet, this periodic increase does not cause leading edge separation. Although not measured, the increase in relative flow angle is expected to increase the blade loading. Hence, it might play a role in the 17.5% increase in pressure rise under the present flow conditions. Increase in relative flow angle caused by the outflow from the grooves is consistent with trends reported by Takata and Tsukuda [4], and Müller et al. [7]. However, the improved performance could also be associated with reduced TLV-induced blockage and/or secondary flows reported in Refs. [5], [7], and [8].

As the blade rotates past the grooves, the circulating flows entrain parts of the TLV, reducing its size and strength, as well as confining its remnants to the downstream corner of the groove. By the time the next blade arrives, the vortex signature essentially vanishes. Furthermore, the grooves prevent the formation of large-scale backflow vortices, which play a key role in the onset of rotating stall in the untreated rotor [29]. These vortices propagate diagonally upstream from the SS of one blade to the PS of the next blade and then to the next passage. Comparisons between the untreated and treated flows reveal likely causes for BFV disappearance in the latter. The BFVs roll up in a region of high radial gradients in circumferential velocity under the TLV, and migrate to the next passage as the TLV grows and migrates away from the blade SS to the PS of the neighboring blade. By sucking the flow with high positive circumferential velocity and reinjecting it back in the negative direction, the grooves constrain the region where the BFVs can form, and prevent them from reaching the leading edge of the next blade. The distributions of turbulent kinetic energy provide statistical evidence that in contrast to the untreated casing, very little turbulence originating from a previous TLV, including the BFVs, propagates from the PS to the SS of the blade across the tip gap. Hence, the high TLV-related turbulence remains confined to the entrance to groove. Elevated, but lower turbulence is also generated as the outflow from the groove is injected into the passage.

Acknowledgment

The authors would like to thank Chunill Hah and Michael Hathaway from NASA Glenn for their guidance, and for modifying the LSAC blade geometries to match the constraints of the JHU index-matched facility. The authors would also like to express their gratitude to Yury Ronzhes who designed all the mechanical components of the test facility and to Andy Breeze-Stringfellow and Ramakrishna Mallina from General Electric for their help in selecting the casing groove geometry.

Funding Data

- Glenn Research Center (Grant No. NMX11AI21A).
- Office of Naval Research (Grant No. N00014-09-1-0353).

Nomenclature

c = rotor blade tip chord
c_A = rotor blade tip axial chord
h = width of the rotor blade tip gap
H = rotor blade span
k = turbulent kinetic energy
L = nominal distance from the hub to the inner casing endwall
p_{exit} = static pressure at stator outlet
p_{in} = static pressure at IGV inlet
r, z, θ = radial, axial and circumferential coordinates
r_{hub} = rotor hub radius
r^* = normalized radial coordinate
s = rotor blade chordwise coordinate
u_r, u_z, u_θ = radial, axial and circumferential velocity
U_T = rotor blade tip speed
u' = velocity fluctuation
ρ = NaI solution density
φ = flow coefficient
ψ_{SS} = static-to-static pressure rise coefficient
Ω = rotor angular velocity
ω_θ = circumferential vorticity
$< >$ = ensemble averaged quantity

References

[1] Moore, R. D., Kovich, G., and Blade, R. J., 1971, "Effect of Casing Treatment on Overall and Blade Element Performance of a Compressor Rotor," National Aeronautics and Space Administration, Ames Research Center, Mountain View, CA, NASA Technical Note No. TN D-6538.
[2] Osborn, W. M., Lewis, G. W. J., and Heidelberg, L. J., 1971, "Effect of Several Porous Casing Treatments on Stall Limit and on Overall Performance of an Axial-Flow Compressor Rotor," National Aeronautics and Space Administration, Washington, DC, NASA Technical Note No. TN D-6537.
[3] Fujita, H., and Takata, H., 1984, "A Study on Configurations of Casing Treatment for Axial Flow Compressors," Bull. JSME, **27**(230), pp. 1675–1681.
[4] Takata, H., and Tsukuda, Y., 1977, "Stall Margin Improvement by Casing Treatment—Its Mechanism and Effectiveness," ASME J. Eng. Power, **99**(1), pp. 121–133.
[5] Smith, G. D. J., and Cumpsty, N. A., 1984, "Flow Phenomena in Compressor Casing Treatment," ASME J. Eng. Gas Turbines Power, **106**(3), pp. 532–541.
[6] Brandstetter, C., Kegalj, M., Wartzek, F., Heinichen, F., and Schiffer, H.-P., 2014, "Stereo PIV Measurement of Flow Structures Underneath an Axial-Slot Casing Treatment on a One and a Half Stage Transonic Compressor," 17th International Symposium on Applications of Laser Techniques to Fluid Mechanics, Lisbon, Portugal, July 7–10, pp. 1–18.
[7] Müller, M. W., Schiffer, H.-P., Voges, M., and Hah, C., 2011, "Investigation of Passage Flow Features in a Transonic Compressor Rotor," ASME Paper No. GT2011-45364.
[8] Crook, A. J., Greitzer, E. M., Tan, C. S., and Adamczyk, J. J., 1993, "Numerical Simulation of Compressor Endwall and Casing Treatment Flow Phenomena," ASME J. Turbomach., **115**(3), pp. 501–512.
[9] Beheshti, B. H., Teixeira, J. A., Ivey, P. C., Ghorbanian, K., and Farhanieh, B., 2004, "Parametric Study of Tip Clearance—Casing Treatment on Performance and Stability of a Transonic Axial Compressor," ASME J. Turbomach., **126**(4), pp. 527–535.
[10] Wilke, I., and Kau, H.-P., 2004, "A Numerical Investigation of the Flow Mechanisms in a High Pressure Compressor Front Stage With Axial Slots," ASME J. Turbomach., **126**(3), pp. 339–349.
[11] Djeghri, N., Vo, H. D., and Yu, H., 2015, "Parametric Study for Losses Casing Treatment on a Mixed-Flow Compressor Rotor," ASME Paper No. GT2015-42750.
[12] Day, I. J., 2016, "Stall, Surge and 75 Years of Research," ASME J. Turbomach., **138**(1), p. 11004.
[13] McDougall, N. M., Cumpsty, N. A., and Hynes, T. P., 1990, "Stall Inception in Axial Compressors," ASME J. Turbomach., **112**(1), pp. 116–123.
[14] Garnier, V. H., Epstein, A. H., and Greitzer, E. M., 1991, "Rotating Waves as a Stall Inception Indication in Axial Compressors," ASME J. Turbomach., **113**(4), pp. 290–301.
[15] Camp, T. R., and Day, I. J., 1998, "A Study of Spike and Modal Stall Phenomena in a Low-Speed Axial Compressor," ASME J. Turbomach., **120**(7), pp. 393–401.
[16] Deppe, A., Saathoff, H., and Stark, U., 2005, "Spike-Type Stall Inception in Axial-Flow Compressors," Sixth European Conference on Turbomachinery, Lille, France, Mar. 7–11, pp. 178–188.
[17] Tan, C. S., Day, I., Morris, S., and Wadia, A., 2010, "Spike-Type Compressor Stall Inception, Detection, and Control," Annu. Rev. Fluid Mech., **42**(1), pp. 275–300.
[18] Vo, H. D., Tan, C. S., and Greitzer, E. M., 2008, "Criteria for Spike Initiated Rotating Stall," ASME J. Turbomach., **130**(1), p. 11023.
[19] Pullan, G., Young, A. M., Day, I. J., Greitzer, E. M., and Spakovszky, Z. S., 2015, "Origins and Structure of Spike-Type Rotating Stall," ASME J. Turbomach., **137**(5), p. 51007.
[20] Hoying, D. A., Tan, C. S., Vo, H. D., and Greitzer, E. M., 1999, "Role of Blade Passage Flow Structures in Axial Compressor Rotating Stall Inception," ASME J. Turbomach., **121**(4), pp. 735–742.
[21] Houghton, T., and Day, I., 2012, "Stability Enhancement by Casing Grooves: The Importance of Stall Inception Mechanism and Solidity," ASME J. Turbomach., **134**(2), p. 21003.
[22] Wu, H., Tan, D., Miorini, R. L., and Katz, J., 2011, "Three-Dimensional Flow Structures and Associated Turbulence in the Tip Region of a Waterjet Pump Rotor Blade," Exp. Fluids, **51**(6), pp. 1721–1737.
[23] Miorini, R. L., Wu, H., and Katz, J., 2012, "The Internal Structure of the Tip Leakage Vortex Within the Rotor of an Axial Waterjet Pump," ASME J. Turbomach., **134**(3), p. 31018.
[24] Tan, D., Li, Y., Wilkes, I., Miorini, R., and Katz, J., 2015, "Visualization and Time-Resolved Particle Image Velocimetry Measurements of the Flow in the Tip Region of a Subsonic Compressor Rotor," ASME J. Turbomach., **137**(4), p. 41007.
[25] Wu, H., Miorini, R. L., and Katz, J., 2011, "Measurements of the Tip Leakage Vortex Structures and Turbulence in the Meridional Plane of an Axial Water-Jet Pump," Exp. Fluids, **50**(4), pp. 989–1003.
[26] Wu, H., Miorini, R. L., Tan, D., and Katz, J., 2012, "Turbulence Within the Tip-Leakage Vortex of an Axial Waterjet Pump," AIAA J., **50**(11), pp. 2574–2587.
[27] Tan, D., Li, Y., Chen, H., Wilkes, I., and Katz, J., 2015, "The Three Dimensional Flow Structure and Turbulence in the Tip Region of an Axial Flow Compressor," ASME Paper No. GT2015-43385.
[28] Li, Y., Chen, H., Tan, D., and Katz, J., 2016, "Effects of Tip Clearance and Operating Conditions on the Flow Structure and Reynolds Stresses Within an Axial Compressor Rotor Passage," ASME Paper No. GT2016-57050.
[29] Chen, H., Li, Y., Tan, D., and Katz, J., 2017, "Visualizations of Flow Structures in the Rotor Passage of an Axial Compressor at the Onset of Stall," ASME J. Turbomach., **139**(4), p. 41008.
[30] Hah, C., Hathaway, M., and Katz, J., 2014, "Investigation of Unsteady Flow Field in a Low-Speed One and a Half Stage Axial Compressor, Part 2: Effects of Tip Gap Size on the Tip Clearance Flow Structure at Near Stall Operation," ASME Paper No. GT2014-27094.
[31] Bai, K., and Katz, J., 2014, "On the Refractive Index of Sodium Iodide Solutions for Index Matching in PIV," Exp. Fluids, **55**(4), pp. 1–6.
[32] Wieneke, B., 2005, "Stereo-PIV Using Self-Calibration on Particle Images," Exp. Fluids, **39**(2), pp. 267–280.
[33] Adrian, R., and Westerweel, J., 2011, *Particle Image Velocimetry*, Cambridge University Press, New York, pp. 241–248.
[34] Roth, G. I., and Katz, J., 2001, "Five Techniques for Increasing the Speed and Accuracy of PIV Interrogation," Meas. Sci. Technol., **12**(3), pp. 238–245.
[35] Westerweel, J., and Scarano, F., 2005, "Universal Outlier Detection for PIV Data," Exp. Fluids, **39**(6), pp. 1096–1100.